

DUT: Learning Video Stabilization by Simply Watching Unstable Videos

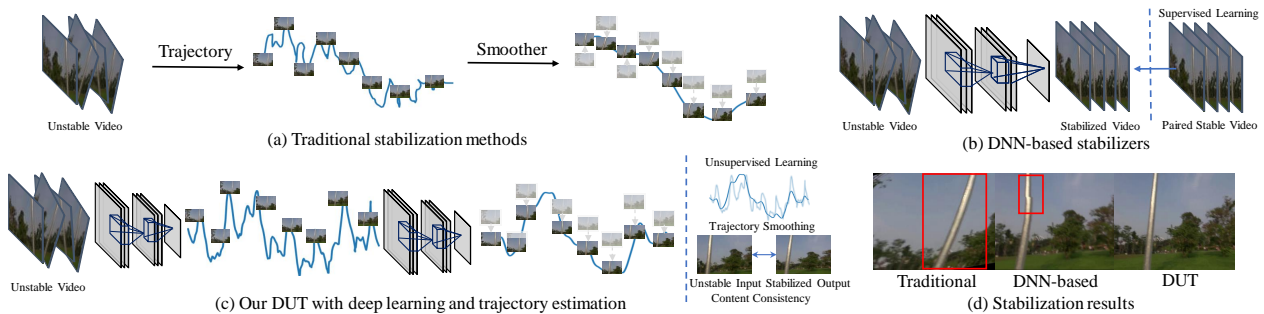
Yufei Xu¹Jing Zhang¹Stephen J. Maybank²Dacheng Tao¹¹UBTECH Sydney AI Centre, Faculty of Engineering, The University of Sydney²Department of Computer Science and Information Systems, Birkbeck College

Figure 1. Comparison of our DUT and other stabilizers. (a) Traditional methods estimate the trajectory using hand-crafted features and smooth it with a fixed-kernel smoother. Stabilized frames are warped from the unstable one (marked in transparent color) according to the smoothed trajectory. (b) DNN-based methods directly generate the stabilized results without explicitly modeling the smoothing process. The pipeline is hard to control and may produce distortion. (c) Our DUT stabilizes videos with explicit trajectory estimation and smoothing using DNNs. (d) Stabilized results of a traditional method [15] (over-crop and shear), DNN-based method [29] (distortion), and DUT.

Abstract

We propose a *Deep Unsupervised Trajectory-based stabilization framework (DUT)* in this paper¹. Traditional stabilizers focus on trajectory-based smoothing, which is controllable but fragile in occluded and textureless cases regarding the usage of hand-crafted features. On the other hand, previous deep video stabilizers directly generate stable videos in a supervised manner without explicit trajectory estimation, which is robust but less controllable and the appropriate paired data are hard to obtain. To construct a controllable and robust stabilizer, DUT makes the first attempt to stabilize unstable videos by explicitly estimating and smoothing trajectories in an unsupervised deep learning manner, which is composed of a DNN-based keypoint detector and motion estimator to generate grid-based trajectories, and a DNN-based trajectory smoother to stabilize videos. We exploit both the nature of continuity in motion and the consistency of keypoints and grid vertices before and after stabilization for unsupervised training. Experiment results on public benchmarks show that DUT outperforms representative state-of-the-art methods both qualitatively and quantitatively.

¹Our code is available at <https://github.com/Annless/DUTCode>.

1. Introduction

Videos captured by amateurs using hand-held cameras are usually shaky, leading to unpleasing visual experiences. Moreover, unstable videos also increase the complexity of subsequent vision tasks, such as object tracking and visual simultaneous localization and mapping (SLAM). Video stabilization is to remove the undesirable shake and generate a stabilized video from the unstable one, thereby improving the visual experience and facilitating down-stream tasks.

Traditional video stabilization methods [14, 15, 16, 17, 18, 19, 32] usually adopt a trajectory-based pipeline consisting of three components: 1) keypoint detection, 2) trajectory estimation based on keypoint tracking, and 3) trajectory smoothing, as illustrated in Figure 1(a). Once the smoothed trajectory is obtained, the stabilized video can be generated by warping the unstable one. However, several challenges degrade these methods. First, the keypoint detector is usually based on hand-crafted features, which are less discriminative and representative in textureless and occluded areas. Second, the keypoint tracker such as the KLT tracker may fail when there is a large appearance variance around keypoints due to occlusion, illumination, viewpoint change, and motion blur as shown in Figure 1(d). Third, a smoother with a fixed kernel is always used for trajectory

smoothing, which cannot adapt to various trajectories with different long- and short-term dynamics.

Recently, some deep learning-based methods have been proposed [3, 8, 29, 31, 33, 34, 37]. Unlike the traditional trajectory-based methods, they prefer to regress the unstable-to-stable transformation or generate the stabilized video directly in an end-to-end manner as illustrated in Figure 1(b). Although they can stabilize videos well, several issues exist here. First, these methods are less controllable and explainable, making it hard to diagnose and improve the network components when there are large unexpected distortion or over-crop [29], *e.g.*, in complex scenes with multiple planar motions as shown in Figure 1(d). Second, training deep models requires large-scale unstable and stable video pairs, which are hard to collect in the real world. Although some methods [3, 34] propose to use pseudo unstable videos, they dismiss the depth variance and dynamic objects in real scenes, thereby introducing a domain gap and impairing the model’s generalization ability.

To address the aforementioned issues, we make the first attempt to stabilize unstable videos by explicitly estimating and smoothing trajectories using unsupervised DNN models as illustrated in Figure 1(c). Specifically, a novel **Deep Unsupervised Trajectory-based stabilizer (DUT)** is proposed, including three neural network modules: keypoint detection (KD), motion propagation (MP), and trajectory smoothing (TS). First, the KD module detects distinct keypoints from unstable image sequences along with their motion vectors calculated by an optical flow network. Next, the MP network propagates the keypoints’ motion to grid vertices on each frame and obtain their trajectories by associating corresponding vertices temporally, which are then smoothed by the TS module. The stabilizer is optimized to estimate the trajectory by exploiting the nature of continuity in motion and smooth the trajectory by keeping the consistency of keypoints and vertices before and after stabilization, leading to an unsupervised learning scheme.

The main contributions of this paper are threefold:

- We propose a novel DUT stabilizer that firstly estimates and smooths trajectories using DNNs, which is more effective than traditional counterparts to handle challenging cases owing to its powerful representation capacity while inheriting the controllable and explainable ability.
- We propose an unsupervised training scheme for stabilization that does not need paired unstable and stable data.
- DUT outperforms state-of-the-art methods both qualitatively and quantitatively on public benchmarks while being light-weight and computationally efficient.

2. Related Work

We briefly review representative traditional (2D and 3D) methods and DNN-based stabilizers as follows.

2D Methods. 2D methods describe the camera path

as 2D motion on the image plane [30, 5]. A typical way is to detect and track keypoints across all the frames and obtain the smoothed temporal trajectory via optimization, such as low-rank approximation [15], L1 norm optimization [7], bundled optimization [18], epipolar geometry [6], and geodesics optimization[36]. These methods need long-term tracked keypoints to estimate complete trajectories, which is challenging due to the appearance variance around keypoints. Recently, motion profile (Mp)-based methods have attracted increasing attentions [16, 19]. Mp describes frame-to-frame 2D motions at specific locations, *e.g.*, dense pixels or sparse vertices from predefined grids, and obtains the trajectories by associating corresponding pixels or vertices across all the frames. Although the Mp-based stabilization pipeline is simple and effective, it may fail in occluded and textureless areas due to the limited ability of hand-crafted features. We also adopt the Mp-based trajectory description but revolutionize the key modules with novel neural ones, which can handle challenging cases by leveraging the powerful representation capacity of DNNs.

3D Methods. 3D methods estimate and smooth camera paths in 3D space and construct point clouds for precise construction and re-projection [35, 9]. For example, Liu *et al.* leverage structure from motion (SfM) [27] to construct 3D camera paths and use content preserving warping to synthesize stabilized frames in [14]. Although this pipeline is appealing since it can describe the exact 3D camera motion, SfM itself is a challenging task that estimating accurate camera poses and 3D point clouds is difficult when there are large occlusions, heavy blur, and dynamic objects. Recently, special hardware is used [17, 23, 11] for precise camera pose estimation and 3D reconstruction from regular videos or 360° videos [26, 12]. However, the need for auxiliary hardware limits their usage scenarios. Although we use Mp to describe 2D trajectory rather than 3D camera path, it indeed follows the “divide-and-conquer” idea by using local 2D planar transformation in each grid as an approximation of the 3D transformation, which is effective in most cases.

DNN-based Methods. Recently, DNN-based video stabilizers have been proposed to directly regress unstable-to-stable transformation from data. Wang *et al.* uses a two branch Siamese network to regress grid-based homography [29]. Xu *et al.* leverage several spatial transformer networks (STN) [10] in the encoder to predict the homography gradually [31]. Huang *et al.* exploit multi-scale features to regress global affine transformation [8]. Although they can obtain stabilized videos, it is difficult for them to adapt to background depth variance and dynamic foreground objects, thereby producing distortion in these cases. Recently, Yu *et al.* leverage a convolutional neural network (CNN) as an optimizer and obtain stabilized video via iteratively training [33], which is computationally inefficient. Choi *et al.* proposes a neighboring frame interpolation method [3],

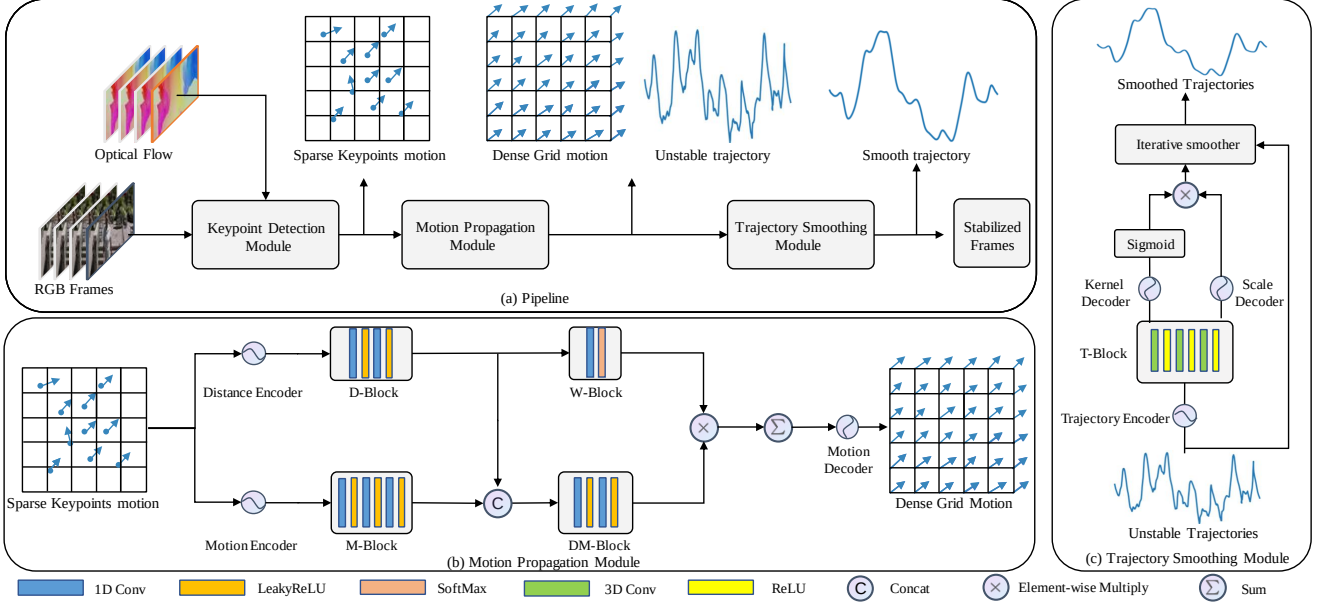


Figure 2. (a) The pipeline of our video stabilization framework, which contains three modules: keypoint detection module, motion propagation module, and trajectory smoothing module. The keypoint detection module utilizes the detector from RFNet [22] and optical flow from PWCNet [25] for motion estimation. (b) The motion propagation module aims to propagate the motions from sparse keypoints to dense grid vertices. It employs two separate branches of stacked 1d convolutions to embed keypoint location and motion features, generate attention vector and attended features to predict the motion vector for each grid vertex. (c) The trajectory smoothing module aims to smooth the estimated trajectories at all grid vertices by predicting smoothing kernel weights. Three 3d convolutions are stacked to process the trajectories both spatially and temporally. The estimated kernel and scale are multiplied to form the final kernel for iterative smoothing.

which can generate stable videos but may also introduce ghost artifacts around dynamic objects. Yu *et al.* introduces a two-stage method [34] that uses optical flow based warping for stabilization while requiring the pre-stabilization result by a traditional method.

By contrast, our DUT method stabilizes unstable videos by explicitly estimating and smoothing trajectories using DNN models. It inherits the controllable and explainable ability from trajectory-based stabilizers while being effective to handle challenging cases owing to the powerful representation capacity. Moreover, it does not require paired data for training.

3. Methods

As shown in Figure 2, given an unstable video as input, DUT aims to generate a stabilized video. It consists of three key modules: 1) keypoint detection, 2) motion propagation, and 3) trajectory smoothing, which are detailed as follows.

3.1. Keypoint Detection (KD)

The keypoint detection module aims to detect keypoints and calculate their motion vectors, which is the preliminary step to construct the motion profile. In this paper, we adopt the RFNet [22] as our keypoint detector, which is trained on the HPatches dataset [1]. Compared with the traditional

keypoint detectors [2, 20, 28] and other deep learning-based ones [4, 21], RFNet can efficiently produce high-resolution response maps for selecting robust keypoints since it adopts a multi-scale and shallow network structure.

Denote the input video as $\{f_i | \forall i \in [1, E]\}$, where f_i is the i th frame of the video and E is the number of frames. The detected keypoints can be expressed as $\{p_{ij} = KD(f_i) | \forall i \in [1, E], \forall j \in [1, L]\}$, p_{ij} is the j th detected keypoint on frame f_i , $KD(\cdot)$ denotes the keypoint detector embodied by RFNet, L is the number of detected keypoints, which is set to 512 in this paper. For simplicity, we use the same symbol p_{ij} to denote the keypoint location without causing ambiguity. Once we obtain the keypoints, we can calculate their motion vectors from the optical flow field. In this paper, we adopt PWCNet [25] to calculate the optical flow. We denote the keypoints and their motion vector as $\{(p_{ij}, m_{ij}) | \forall i \in [1, E - 1], \forall j \in [1, L]\}$, where m_{ij} denotes the motion vector of the keypoint p_{ij} on frame f_i .

3.2. Motion Propagation (MP)

3.2.1 CNN-based Motion Propagation

Since there are always multiple planar motions existing in the real-world unstable videos due to background depth variance and dynamic foreground objects, using a single global homograph to model the frame-to-frame transforma-

tion or unstable-to-stable transformation is inaccurate. To address this issue, we adopt the grid-based motion profiles to describe the motions. Specifically, each frame is uniformly divided into a fixed set of grids, *i.e.*, $M \times N$ grids in this paper. The local motion within each grid is treated as a planar motion, which is reasonable. It can be described by a frame-to-frame homograph transformation derived from the motion vectors of grid vertices. However, we only have the motion vectors of keypoints distributed in these local grids. How to propagate the motion vectors to each grid vertex is challenging. In contrast to existing methods, which use a median filter to estimate the motion vector of each vertex from its neighboring keypoints, we devise a novel motion propagation module based on DNNs by exploiting the nature of continuity in motion, which can obtain more robust and accurate motion vectors for each grid.

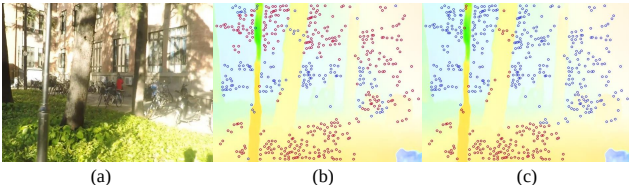


Figure 3. (a) An input image. (b) Inliers (red points) and outliers (blue points) identified using the single-homography estimation with RANSAC. (c) Two clusters of keypoints identified by our multi-homography estimation method based on K-means. The background of (b) and (c) is the visualized optical flow field of (a).

Specifically, we adopt the idea in [16] by propagating the residual motion vectors. In [16], they use a global homography transformation to calculate the reference motion vector of each keypoint and then calculate the residual. However, there may be multiple planar motions as shown in Figure 3(b), thereby estimating a single homography leads to shear artifacts and large residuals. In this paper, we propose a multi-homography estimation method to calculate more suitable residuals with lower amplitudes, thereby facilitating the subsequent motion propagation process.

As shown in Figure 3(c), we first employ K-means [13] on $\{m_{ij}\}$ to divide the keypoints on f_i into two clusters, *i.e.*, $C_i^c = \{(p_{ij}, m_{ij}) | \forall j \in \Lambda_i^c\}$, where $c = 0$ or 1 denotes the cluster index and Λ_i^c is the keypoint index set belonging to the cluster C_i^c . Note that when the number of keypoints in any cluster is less than a threshold, *i.e.*, $20\% \times L = 102$ in this paper, we merge it into the master cluster. Then, we can estimate the global homography transformation for each cluster, denoting H_i^c . The residual motion vector Δm_{ij} of each keypoint can be formulated as:

$$\Delta m_{ij} = p_{ij} + m_{ij} - H_i^c(p_{ij}), \forall j \in \Lambda_i^c. \quad (1)$$

Given Δm_{ij} and the distance vector d_{ijk} between each grid vertex v_{ik} and keypoint p_{ij} , *i.e.*, $d_{ijk} = p_{ij} - v_{ik}$,

$k = 1, \dots, MN$, the motion propagation module predicts the residual motion vector Δn_{ik} for each vertex v_{ik} , *i.e.*

$$\Delta n_{ik} = MP(\{(\Delta m_{ij}, d_{ijk}) | \forall j \in [1, L]\}), \quad (2)$$

where $MP(\cdot)$ denotes the proposed MP network. The distance vectors and motion vectors of size $[MN, L, 2]$ (after tiling) are fed into two separate encoders as shown in Figure 2(b). The encoded features are further embedded by several 1D convolutions. Then, the attention vector of size $[MN, L, 1]$ is obtained based on the distance embeddings and used to aggregate the features from concatenated motion embeddings and distance embeddings, generating the attended feature of size $[MN, 1, 2]$, which is further used to predict the final dense residual motions Δn_{ik} through a motion decoder. Details of the MP network can be found in the supplementary material. Then we can calculate the target motion vector n_{ik} of each vertex v_{ik} as follows by referring to Eq. (1),

$$n_{ik} = \Delta n_{ik} + (H_i^c(v_{ik}) - v_{ik}), \quad (3)$$

Note that we reuse the same symbol v_{ik} to denote the grid vertex location for simplicity like p_{ij} . Besides, we choose H_i^c for each vertex v_{ik} according to the majority cluster index of its neighboring keypoints in Ω_{ik} , which is defined as $\Omega_{ik} = \{j | \|d_{ijk}\|_2 \leq R\}$. Here, R is a predefined radius, *i.e.*, 200 pixels in this paper. Unlike [16], which only uses a median filter to obtain the residual motion of each vertex from its neighboring keypoints' residual motion vectors, *i.e.*, $\Delta n_{ik} = \text{MedianFilter}(\{\Delta m_{ij} | \forall j \in \Omega_{ik}\})$, the proposed neural network can model the characteristics of all keypoint residual motion vectors and learn representative features to eliminate noise and predict accurate target residual motion vectors, thereby outperforming the median filter by a large margin as demonstrated in the experiments.

3.2.2 Objective Function

For the estimation of target motion vector n_{ik} of each vertex v_{ik} , there are two constraints on it based on the assumption of local motion continuity. First, n_{ik} should be close to the motion vectors of v_{ik} 's neighboring keypoints. Second, the target position for each keypoint p_{ij} can be calculated based on its motion vector m_{ij} or its projection by the homography transformation of the grid that contains p_{ij} , which can be derived from the four grid vertices' motion vectors [16, 24]. Based on the above two constraints, we formulate the objective function for the MP module as:

$$L_{vm} = \lambda_m \sum_{i=1}^{E-1} \sum_{k=1}^{MN} \sum_{j \in \Omega_{ik}} \|n_{ik} - m_{ij}\|_1 + \lambda_v \sum_{i=1}^{E-1} \sum_{j=1}^L \|p_{ij} + m_{ij} - H_{ij}(p_{ij})\|_2^2, \quad (4)$$

where $\|\cdot\|_1$ denotes the L1 norm, $\|\cdot\|_2$ denotes the L2 norm, H_{ij} is the homography of the grid containing p_{ij} , $\lambda_{m/v}$ is the weight to balance the two terms. If $\lambda_v = 0$, the objective function indeed leads to a median filter solution. In addition to the keypoints-related constraints in Eq. (4), we also introduce a shape preserving loss L_{sp} on each grid g_{im} , *i.e.*,

$$L_{sp} = \sum_{i=1}^{E-1} \sum_{m=1}^{(M-1)(N-1)} \|\hat{v}_{im}^3 - (\hat{v}_{im}^2 + R_{90}(\hat{v}_{im}^1 - \hat{v}_{im}^2))\|_2^2, \quad (5)$$

where $\hat{v}_{im}^o = v_{im}^o + n_{im}^o$, $o = 1, 2, 3, 4$, $v_{im}^1 \sim v_{im}^4$ denote four vertices of g_{im} in the clockwise direction, their motion vectors are $n_{im}^1 \sim n_{im}^4$, $R_{90}(\cdot)$ denotes rotation 90° of a vector. L_{sp} accounts for spatial smoothness and avoids large distortion in textureless regions. The final objective is:

$$L_{MP} = L_{vm} + \lambda_s L_{sp}, \quad (6)$$

where λ_s is loss weight that balances the two losses.

3.3. Trajectory Smoothing (TS)

3.3.1 Jacobi Solver-based Smoother

Associating the motion vectors of corresponding grid vertices on each frame formulates the trajectories, *i.e.*, $T_k = \{t_{ik} = \sum_{m=1}^i n_{mk} | \forall i \in [1, E]\}$ [19, 16]. A typical way to smooth the trajectory is using the Jacobi Solver [19, 16, 18]. The smoothed trajectory should be locally smooth but close to the unstable one, which can be obtained by minimizing the following temporal smoothness loss L_{ts} :

$$L_{ts} = \sum_{i=1}^{E-1} (\|\widehat{T}_{ik} - T_{ik}\|_2^2 + \lambda \sum_{j \in \Omega_i} w_{ij} \|\widehat{T}_{ik} - \widehat{T}_{jk}\|_2^2), \quad (7)$$

where \widehat{T}_{ik} denotes the smoothed trajectory at v_{ik} , w_{ij} is the weight controlling the local smoothness of the trajectory, λ balances the first data term and the second smoothness term, Ω_i is the temporal neighborhood of f_i , *i.e.*, $\Omega_i = [i-3, i+3]$ in this paper. Eq. (7) is a quadratic optimization problem that can be solved by applying the Jacobi Solver iteratively:

$$\widehat{T}_{ik}^t = \frac{T_{ik} + \lambda \sum_{j \in \Omega_i} w_{ij} \widehat{T}_{jk}^{t-1}}{1 + \lambda \sum_{j \in \Omega_i} w_{ij}}, \quad (8)$$

where t denotes the number of iterations. However, the kernel weight w_{ij} of the Jacobi Solver is fixed regardless of the local temporal dynamics of the trajectory. Besides, there are no spatial constraints on the trajectory in Eq (7), which may result in distortion in the final stabilized video.

3.3.2 CNN-based Smoother

To address the above issues, we propose a novel CNN-based smoother that can generate dynamic smoothing kernels based on the characteristics of the trajectories. As

shown in Figure 2(c), the trajectory of size $[2, E, M, N]$ goes through the trajectory encoder with a 1×1 convolution layer. The encoded feature of size $[64, E, M, N]$ is fed into several 3D convolution layers for further embedding, which then goes through a kernel decoder and a scale decoder in parallel, generating features of size $[12, E, M, N]$. The scale decoder output imitates the parameter λ in Eq. (8) while the kernel decoder generates smoothing kernels for each vertex. To keep consistent with Eq. (8), the neighborhood radius is 3. Thereby, there are 12 weights for each vertex since we generate different weights for different dimensions. The generated weights are used for smoothing the trajectory according to Eq. (8).

3.3.3 Objective Function

To supervise the training of the CNN smoother, we devise an objective function by considering both spatial and temporal smoothness as well as a content preserving loss, *i.e.*,

$$L_{TS} = L_{ts} + \lambda_s L_{sp} + \lambda_c L_{cp}, \quad (9)$$

where L_{ts} is same as defined in Eq. (7), L_{sp} is the spatial shape preserving loss similar to the one used for MP in Eq. (5) where the target position of v_{ik} after smoothing is:

$$\hat{v}_{ik} = v_{ik} + \widehat{T}_{ik} - T_{ik}. \quad (10)$$

Moreover, since distortion in structural areas around keypoints affects the visual experience more than those in textureless areas, we introduce a content preserving loss L_{cp} :

$$L_{cp} = \sum_{i=1}^{E-1} \sum_{j=1}^L \|Bili(p_{ij}) - H_{ij}(p_{ij})\|_2^2, \quad (11)$$

where H_{ij} is same as in Eq. (4). Assuming p_{ij} is in the grid g_{im} , then $Bili(\cdot)$ denotes a bilinear interpolation, *i.e.*, $Bili(p_{ij}) = \sum_{o=1}^4 w_o \hat{v}_{im}^o$. Here, $\hat{v}_{im}^1 \sim \hat{v}_{im}^4$ are the target positions of four vertices in g_{im} after smoothing and calculated as Eq. (10). $w_1 \sim w_4$ are the interpolation coefficients calculated based on the position of p_{ij} relative to the four vertices of g_{im} before smoothing, *i.e.*, $v_{im}^1 \sim v_{im}^4$. L_{cp} indeed preserves the shape of each grid containing keypoints, which probably has structural content. Note that the proposed CNN smoother can be trained using only unstable videos based on the objective in Eq. (9). In conclusion, the stabilization process can be summarized in Algorithm 1.

4. Experiments

We evaluated our model on public benchmark dataset NUS [18] and compared it with state-of-the-art video stabilization methods, including deep learning-based method [29, 3] and traditional methods [15, 16]. Both quantitative and qualitative results as well as model complexity are provided for comprehensive comparison. Ablation studies of key modules in our model were also conducted.

Algorithm 1: Deep Unsupervised Trajectory-based Video Stabilizer (DUT)

Input: Unstable video: $\{f_i | i \in [1, E]\}$
Optical flow: $\{OF_i | i \in [1, E - 1]\}$;
Output: Stabilized video: $\{\hat{f}_i | i \in [1, E]\}$
Grid motion: $\{n_{ik} | i \in [1, E - 1], k \in [1, MN]\}$
Estimated trajectory: $\{T_k | k \in [1, MN]\}$
Smoothed trajectory: $\{\hat{T}_k | k \in [1, MN]\}$;

for $i = 1 : E - 1$ **do**
 $\{p_{ij} | j \in [1, L]\} = RFN_{et}(f_i); \forall j, m_{ij} = OF_i(p_{ij});$
 if *There are multiple planes in frame f_i* **then**
 $H_i^c = MultiHomo(\{p_{ij} | \forall j\}, \{m_{ij} | \forall j\});$
 else
 $H_i^c = SingleHomo(\{p_{ij} | \forall j\}, \{m_{ij} | \forall j\});$
 end
 $\Delta m_{ij} = p_{ij} + m_{ij} - H_i^c(p_{ij}), \forall j \in \Lambda_i^c;$
 for $k = 1 : MN$ **do**
 $d_{ijk} = p_{ij} - v_{ik}, \forall j \in [1, L];$
 $\Delta n_{ik} = MP(\{(\Delta m_{ij}, d_{ijk}) | \forall j \in [1, L]\});$
 $n_{ik} = \Delta n_{ik} + (H_i^c(v_{ik}) - v_{ik});$
 end
end
for $k = 1 : MN$ **do**
 $T_k = \sum_{i=1}^{E-1} n_{ik}; \hat{T}_k = Smoother(T_k);$
end
for $i = 0 : E$ **do**
 $\hat{f}_i = Reprojection(f_i, \{T_k | \forall k\}, \{\hat{T}_k | \forall k\})$
end

4.1. Experiment Settings

Unstable videos from DeepStab [29] were used for training. Five categories of unstable videos from [18] were used as the test set. The metrics introduced in [18] were used for quantitative evaluation, including cropping ratio, distortion, and stability. Cropping ratio measures the ratio of remaining area and distortion measures the distortion level after stabilization. Stability measures how stable a video is by frequency domain analysis. All the metrics are in the range of $[0, 1]$. A larger value denotes a better performance. More implementation details, user study results, and robustness evaluation can be found in the supplementary material.

4.2. Quantitative Results

Table 1. Stability scores of different methods.

	Regular	Parallax	Running	QuickRot	Crowd	Avg.
Meshflow	<u>0.843</u>	0.793	<u>0.839</u>	0.801	0.774	0.810
SubSpace	0.837	0.760	0.829	\	0.730	0.789*
DIFRINT	0.838	<u>0.808</u>	0.822	<u>0.835</u>	<u>0.791</u>	<u>0.819</u>
StabNet	0.838	0.769	0.818	0.785	0.741	0.790
DUT	0.843	0.813	0.841	0.877	0.792	0.833

* The average score is not accurate since SubSpace fails to stabilize some of the videos in the category of Quick Rotation.

Table 2. Distortion scores of different methods.

	Regular	Parallax	Running	QuickRot	Crowd	Avg.
Meshflow	0.898	0.716	0.764	<u>0.763</u>	0.756	0.779
SubSpace	<u>0.973</u>	0.855	0.939	\	0.831	0.900
DIFRINT	0.934	<u>0.921</u>	0.873	0.633	<u>0.905</u>	0.853
StabNet	0.702	0.573	0.753	0.574	0.759	0.672
DUT	0.982	0.949	<u>0.927</u>	0.935	0.955	0.949

Table 3. Cropping ratios of different methods.

	Regular	Parallax	Running	QuickRot	Crowd	Avg.
Meshflow	0.686	0.540	0.584	0.376	0.552	0.548
SubSpace	0.712	0.617	0.686	\	0.543	0.639
DIFRINT	0.922	0.903	0.869	0.732	0.882	0.862
StabNet	0.537	0.503	0.512	0.418	0.497	0.493
DUT	<u>0.736</u>	<u>0.709</u>	<u>0.690</u>	<u>0.673</u>	<u>0.710</u>	<u>0.704</u>

We compared our method with representative state-of-the-art video stabilization methods, including traditional methods: Subspace [15], Meshflow [16], and deep learning methods: DIFRINT [3] and StabNet [29]. The quantitative results are summarized in Table 1. There are several empirical findings. **Firstly**, the proposed DUT stabilizer achieves better performance in challenging cases with multiple planar motions, *e.g.*, in the category of Parallax. Compared with Meshflow [16], DUT has less distortion indicated by the distortion metric, owing to the introduction of multi-homography estimation. **Secondly**, the deep learning-based keypoint detector empowers DUT with better capacity in dealing with challenging cases compared with other traditional stabilizers. In the category of Quick Rotation, which contains blur and large motion in the scenes, DUT still obtains a large margin over other stabilizers regarding distortion and stability metrics. Subspace [15] even fails for videos in this category since it is difficult to track long-term robust keypoints. **Thirdly**, compared with StabNet [29], DUT produces less distortion and keeps more areas after cropping. Although StabNet also uses grid-based warping while being trained with paired data from the deepStab dataset, it does not achieve a balance between stability and distortion. By contrast, DUT simply uses unstable videos for training. As there are many possible stabilized videos that all look stable about the same, training with paired data that only provides one single stable instance for each sample may be biased. Besides, the supervisory signal from the stable video is less effective than those from the grid-based pipeline, which have explicit relationships to stability, *e.g.*, displacement derived from the grid motion and trajectory. **Fourthly**, compared with the interpolation-based DIFRINT [3], DUT produces less distortion around the dynamic objects since it can handle them via robust keypoint-based local grid warping. Generally, DUT achieves the best performance regarding stability and distortion, which confirms the superiority of our trajectory-based DNN stabilizer.

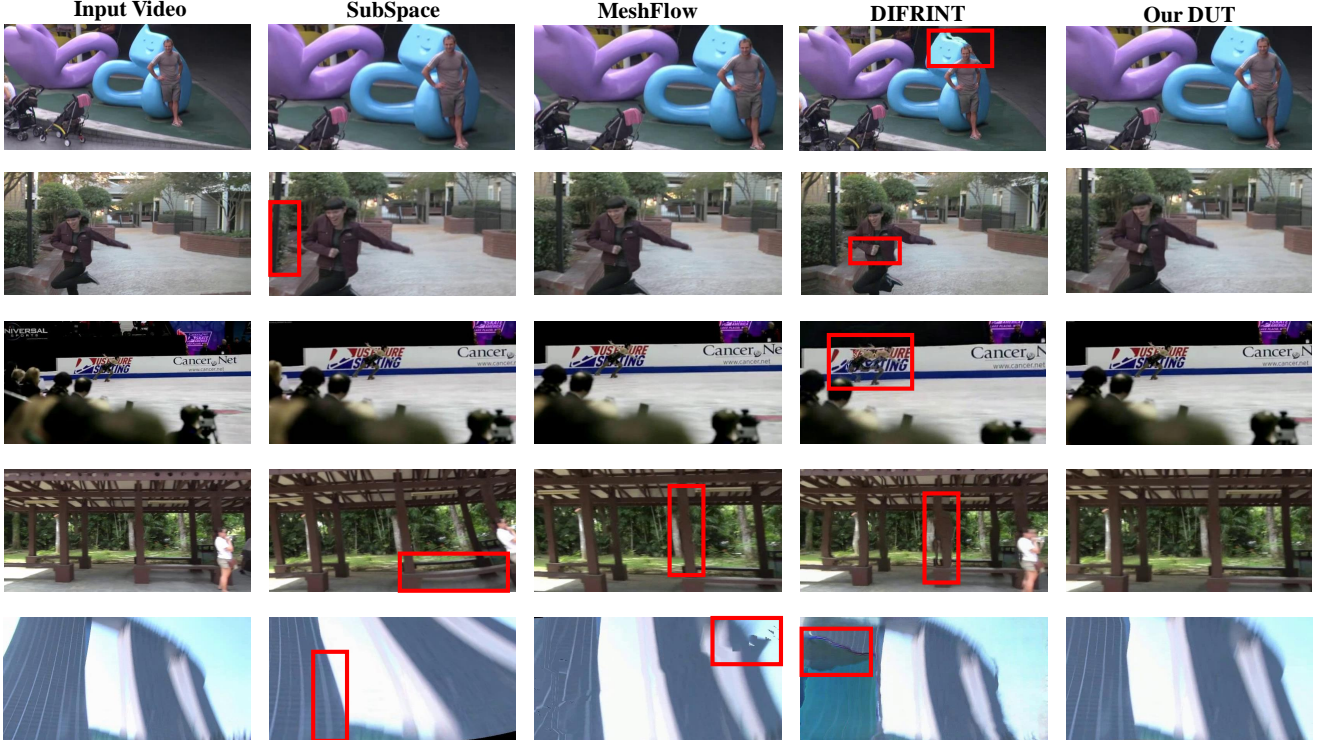


Figure 4. Visual comparison between our DUT and SubSpace [15], Meshflow [16], DIFRINT [3]. We present five kinds of videos for subjective evaluation, *i.e.*, 1) moderate camera shake , 2) large dynamic objects, 3) small dynamic objects, 4) multiple planar motions, and 5) quick camera rotation and blur in the first row to the fifth row, respectively. It can be observed that our method can handle diverse scenarios compared with traditional stabilizers and deep learning-based methods. More results can be found in the supplementary video.

4.3. Subjective Results

Some visual results of different methods are shown in Figure 4. For videos containing dynamic objects (the 1st-3rd rows), DIFRINT [3] is prone to produce ghost artifacts around dynamic objects due to the neighboring frame interpolation, which is unaware of dynamic foregrounds. Subspace [15] may generate some distortion if the dynamic object is large as in the 2nd row. For scenes containing parallax and occlusion (the 4th row), Subspace also produces distortion due to the inaccurate feature trajectory. DIFRINT generates hollows since the interpolation cannot hallucinate the occluded objects. Meshflow [16] produces shear artifacts due to the inaccurate homography estimated from a single plane. DUT has no such drawbacks since it adopts an adaptive multi-homography estimation method. For videos containing quick camera rotation and large blur (the 5th row), Subspace and Meshflow produce strong distortion due to the inaccurate trajectory estimation based on hand-crafted features. There is a dark patch in DIFRINT’s result, which is caused by interpolating far away regions from adjacent frames to the inaccurate area of the current frame due to the quick camera motion. In conclusion, DUT is robust to different camera motion patterns and diverse scenes, owing to its powerful representation capacity of DNNs.

4.4. Ablation Studies

4.4.1 Motion Propagation Module

Since the motion propagation module is crucial for the trajectory smoother by providing accurate grid motions, we compared our MP network with traditional median filter (MF)-based method. Since we did not have ground truth grid motion, we warped the future frame from the current frame based on the estimated grid motions and carried out the evaluation based on the warped frame and ground truth frame. Specifically, we calculated the homography between them and used two metrics related to it for evaluation. First, if the grid motion is accurate, the warped frame should be close to the ground truth frame, *i.e.*, an identity homography. We calculated the Frobenius Norm of the difference between the estimated homography and the identity matrix as the first metric: distance. Second, following [18], we calculated the ratio between the largest two eigenvalues of the homography as the distortion metric, *i.e.*, larger is better.

Table 4. Comparison of Motion Propagation Methods.

	MF-S	MF-M	MP-S	MP-M
Distance↓	0.073	0.034	0.032	0.029
Distortion↑	0.913	0.918	0.919	0.921

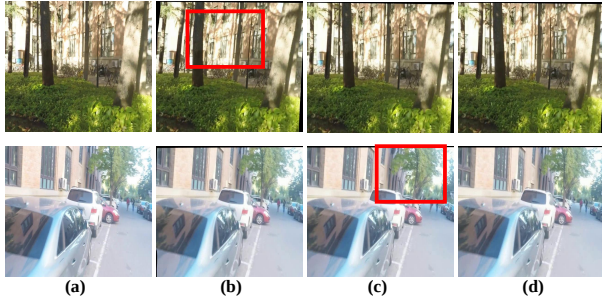


Figure 5. (a) Input images. (b) Motion estimation using single-homography with median filter causes shear artifacts. (c) Using multi-homography with median filter avoids the shear issue but causes distortion. (d) Our MP module can address both issues.

The results are summarized in Table 4. We use ‘‘S’’ and ‘‘M’’ to denote the single- and multi-homography estimation method, respectively. As can be seen, using the proposed multi-homography estimation for calculating the reference motion vectors is more effective than single-homography estimation in both MF and our MP methods. Besides, the proposed MP network outperforms MF consistently no matter which homography estimation is used. As shown in Figure 5, when there are multiple planar motions, using multi-homography estimation can address the shear artifacts in Figure 5(c) caused by the inaccurate single-homography estimation and using the proposed MP network can reduce distortion in Figure 5(d) caused by MF, which only uses neighboring keypoints’ motions for estimation.

4.4.2 Trajectory Smoothing Module

Table 5. Comparison for Jacobi Solver and Smoothing Module.

	Stability	Distortion	CroppingRatio	Time (ms)
Jacobi-100	0.831	0.946	0.702	0.91
DUT-15	0.833	0.949	0.704	0.23

We list the comparison results between the traditional Jacobi Solver-based smoother and our CNN-based smoother in Table 5. As can be seen, even if much less iterations are used, our CNN-based smoother is more effective than the Jacobi Solver in all metrics. It demonstrates that the predicted unique kernel weight for each vertex according to the trajectory is more effective than the fixed one used in the Jacobi Solver, since it can adapt to the dynamics of the trajectory. In this sense, it is ‘‘content-aware’’, where the kernel weight in the Jacobi Solver only depends on temporal distances. Moreover, the proposed CNN-based smoother costs less time, *i.e.*, only 1/4 of that of the Jacobi Solver.

4.5. Model Complexity Comparison

The running time, number of parameters, and number of computations of both traditional and deep learning methods

Table 6. Model Complexity of Different Methods.

	Subspace	StabNet	DIFRINT	DUT
Per-frame (ms)	140	58	364	71
Params (M)	\	30.39	9.94	0.63
FLOPs (G)	\	47.55	67.78	30.42



Figure 6. Failure case of our stabilizer, *e.g.*, one of the planes is texture-less. Using optimal threshold can correct the distortion.

are summarized in Table 6. For a fair comparison, we run Subspace [15], StabNet [29], DIFRINT [3] and our DUT on a 640*480 video with 247 frames for 20 times and calculate the average per frame time cost. DUT has fewer parameters and computations, outperforming all other methods. Besides, it is much faster than Subspace and DIFRINT while being only slightly slower than StabNet.

4.6. Limitations and Discussion

DUT inherits the explainable and controllable ability of the trajectory-based pipeline. Nevertheless, there are some parameters that can be carefully tuned further, *e.g.*, the number of smoothing iterations for different types of videos. Although our CNN-based smoother can predict unique kernel weight for each vertex from the trajectory, more effort can be made, *e.g.*, exploiting attention in the network. Besides, although we propose the idea of multi-homography estimation and demonstrate its effectiveness, if one of the planes is texture-less as in Figure 6, our method may degenerate to the single-homography estimation, resulting in distortion. A carefully tuned threshold can correct the distortion.

5. Conclusion

We propose a novel method DUT for video stabilization by explicitly estimating and smoothing trajectories with DNNs for the first time. DUT outperforms traditional methods by leveraging the representation power of DNNs while inheriting their explainable and controllable ability. With the proposed motion propagation network and CNN-based smoother, it can be trained in an unsupervised manner and generate stabilized video with less distortion, compared with other deep learning stabilizers. Experiments on popular benchmark datasets confirm the superiority of DUT over state-of-the-art methods in terms of both objective metrics and subjective visual evaluation. Moreover, it is lightweight and computationally efficient. More effort can be made to improve the performance of DUT further, *e.g.*, devising an adaptive multi-plane segmentation network.

References

- [1] Vassileios Balntas, Karel Lenc, Andrea Vedaldi, and Krystian Mikolajczyk. Hpatches: A benchmark and evaluation of handcrafted and learned local descriptors. In *Proceedings of the IEEE Conference on Computer Vision and Pattern Recognition*, pages 5173–5182, 2017. [3](#)
- [2] Herbert Bay, Tinne Tuytelaars, and Luc Van Gool. Surf: Speeded up robust features. In *Proceedings of the European Conference on Computer Vision*, pages 404–417, 2006. [3](#)
- [3] Jinsoo Choi and In So Kweon. Deep iterative frame interpolation for full-frame video stabilization. *ACM Transactions on Graphics (TOG)*, 39(1), 2020. [2](#), [5](#), [6](#), [7](#), [8](#), [16](#)
- [4] Daniel DeTone, Tomasz Malisiewicz, and Andrew Rabinovich. Superpoint: Self-supervised interest point detection and description. In *Proceedings of the IEEE Conference on Computer Vision and Pattern Recognition Workshops*, pages 224–236, 2018. [3](#), [11](#)
- [5] Michael L Gleicher and Feng Liu. Re-cinematography: Improving the camerawork of casual video. *ACM transactions on multimedia computing, communications, and applications (TOMM)*, 5(1):1–28, 2008. [2](#)
- [6] Amit Goldstein and Raanan Fattal. Video stabilization using epipolar geometry. *ACM Transactions on Graphics (TOG)*, 31(5):1–10, 2012. [2](#)
- [7] Matthias Grundmann, Vivek Kwatra, and Irfan Essa. Auto-directed video stabilization with robust 11 optimal camera paths. In *Proceedings of the IEEE Conference on Computer Vision and Pattern Recognition*, pages 225–232, 2011. [2](#)
- [8] Chia-Hung Huang, Hang Yin, Yu-Wing Tai, and Chi-Keung Tang. Stablenet: Semi-online, multi-scale deep video stabilization. *arXiv preprint arXiv:1907.10283*, 2019. [2](#)
- [9] Zhiyong Huang, Fazhi He, Xiantao Cai, Yuan Chen, and Xiao Chen. A 2d-3d hybrid approach to video stabilization. In *2011 12th International Conference on Computer-Aided Design and Computer Graphics*, pages 146–150. IEEE, 2011. [2](#)
- [10] Max Jaderberg, Karen Simonyan, Andrew Zisserman, et al. Spatial transformer networks. In *Advances in neural information processing systems*, pages 2017–2025, 2015. [2](#)
- [11] Alexandre Karpenko, David Jacobs, Jongmin Baek, and Marc Levoy. Digital video stabilization and rolling shutter correction using gyroscopes. *CSTR*, 1(2):13, 2011. [2](#)
- [12] Johannes Kopf. 360 video stabilization. *ACM Transactions on Graphics (TOG)*, 35(6):1–9, 2016. [2](#)
- [13] K Krishna and M Narasimha Murty. Genetic k-means algorithm. *IEEE Transactions on Systems, Man, and Cybernetics, Part B (Cybernetics)*, 29(3):433–439, 1999. [4](#)
- [14] Feng Liu, Michael Gleicher, Hailin Jin, and Aseem Agarwala. Content-preserving warps for 3d video stabilization. *ACM Transactions on Graphics (TOG)*, 28(3):1–9, 2009. [1](#), [2](#)
- [15] Feng Liu, Michael Gleicher, Jue Wang, Hailin Jin, and Aseem Agarwala. Subspace video stabilization. *ACM Transactions on Graphics (TOG)*, 30(1):1–10, 2011. [1](#), [2](#), [5](#), [6](#), [7](#), [8](#), [16](#)
- [16] Shuaicheng Liu, Ping Tan, Lu Yuan, Jian Sun, and Bing Zeng. Meshflow: Minimum latency online video stabilization. In *Proceedings of the European Conference on Computer Vision*, pages 800–815, 2016. [1](#), [2](#), [4](#), [5](#), [6](#), [7](#), [16](#)
- [17] Shuaicheng Liu, Yinting Wang, Lu Yuan, Jiajun Bu, Ping Tan, and Jian Sun. Video stabilization with a depth camera. In *Proceedings of the European Conference on Computer Vision*, pages 89–95, 2012. [1](#), [2](#)
- [18] Shuaicheng Liu, Lu Yuan, Ping Tan, and Jian Sun. Bundled camera paths for video stabilization. *ACM Transactions on Graphics (TOG)*, 32(4):1–10, 2013. [1](#), [2](#), [5](#), [6](#), [7](#), [12](#), [15](#), [16](#)
- [19] Shuaicheng Liu, Lu Yuan, Ping Tan, and Jian Sun. Steadyflow: Spatially smooth optical flow for video stabilization. In *Proceedings of the IEEE Conference on Computer Vision and Pattern Recognition*, pages 4209–4216, 2014. [1](#), [2](#), [5](#), [11](#)
- [20] Pauline C Ng and Steven Henikoff. Sift: Predicting amino acid changes that affect protein function. *Nucleic acids research*, 31(13):3812–3814, 2003. [3](#)
- [21] Yuki Ono, Eduard Trulls, Pascal Fua, and Kwang Moo Yi. Lf-net: learning local features from images. In *Advances in neural information processing systems*, pages 6234–6244, 2018. [3](#), [11](#)
- [22] Xuelun Shen, Cheng Wang, Xin Li, Zenglei Yu, Jonathan Li, Chenglu Wen, Ming Cheng, and Zijian He. Rf-net: An end-to-end image matching network based on receptive field. In *Proceedings of the IEEE Conference on Computer Vision and Pattern Recognition*, pages 8132–8140, 2019. [3](#), [11](#), [16](#)
- [23] Brandon M Smith, Li Zhang, Hailin Jin, and Aseem Agarwala. Light field video stabilization. In *Proceedings of the IEEE International Conference on Computer Vision*, pages 341–348, 2009. [2](#)
- [24] Deqing Sun, Stefan Roth, and Michael J Black. Secrets of optical flow estimation and their principles. In *Proceedings of the IEEE Conference on Computer Vision and Pattern Recognition*, pages 2432–2439, 2010. [4](#)
- [25] Deqing Sun, Xiaodong Yang, Ming-Yu Liu, and Jan Kautz. Pwc-net: Cnns for optical flow using pyramid, warping, and cost volume. In *Proceedings of the IEEE Conference on Computer Vision and Pattern Recognition*, pages 8934–8943, 2018. [3](#), [16](#)
- [26] Chengzhou Tang, Oliver Wang, Feng Liu, and Ping Tan. Joint stabilization and direction of 360\deg videos. *arXiv preprint arXiv:1901.04161*, 2019. [2](#)
- [27] Shimon Ullman. The interpretation of structure from motion. *Proceedings of the Royal Society of London. Series B. Biological Sciences*, 203(1153):405–426, 1979. [2](#)
- [28] Deepak Geetha Viswanathan. Features from accelerated segment test (fast). In *Proceedings of the 10th workshop on Image Analysis for Multimedia Interactive Services, London, UK*, pages 6–8, 2009. [3](#), [16](#)
- [29] Miao Wang, Guo-Ye Yang, Jin-Kun Lin, Song-Hai Zhang, Ariel Shamir, Shao-Ping Lu, and Shi-Min Hu. Deep online video stabilization with multi-grid warping transformation learning. *IEEE Transactions on Image Processing*, 28(5):2283–2292, 2018. [1](#), [2](#), [5](#), [6](#), [8](#), [11](#)
- [30] Yu-Shuen Wang, Feng Liu, Pu-Sheng Hsu, and Tong-Yee Lee. Spatially and temporally optimized video stabilization.

- IEEE transactions on visualization and computer graphics*, 19(8):1354–1361, 2013. 2
- [31] Sen-Zhe Xu, Jun Hu, Miao Wang, Tai-Jiang Mu, and Shi-Min Hu. Deep video stabilization using adversarial networks. In *Computer Graphics Forum*, volume 37, pages 267–276. Wiley Online Library, 2018. 2
- [32] Jiyang Yu and Ravi Ramamoorthi. Selfie video stabilization. In *Proceedings of the European Conference on Computer Vision (ECCV)*, pages 551–566, 2018. 1
- [33] Jiyang Yu and Ravi Ramamoorthi. Robust video stabilization by optimization in cnn weight space. In *Proceedings of the IEEE Conference on Computer Vision and Pattern Recognition*, pages 3800–3808, 2019. 2
- [34] Jiyang Yu and Ravi Ramamoorthi. Learning video stabilization using optical flow. In *Proceedings of the IEEE Conference on Computer Vision and Pattern Recognition*, pages 8159–8167, 2020. 2, 3
- [35] Guofeng Zhang, Wei Hua, Xueying Qin, Yuanlong Shao, and Hujun Bao. Video stabilization based on a 3d perspective camera model. *The Visual Computer*, 25(11):997, 2009. 2
- [36] Lei Zhang, Xiao-Quan Chen, Xin-Yi Kong, and Hua Huang. Geodesic video stabilization in transformation space. *IEEE Transactions on Image Processing*, 26(5):2219–2229, 2017. 2
- [37] Minda Zhao and Qiang Ling. Pwstabilenet: Learning pixel-wise warping maps for video stabilization. *IEEE Transactions on Image Processing*, 29:3582–3595, 2020. 2

Appendices

A. Detailed Network Structure

Table 7. Detailed structure of our DUT model.

DUT Structure		
Block Name	Output Size	Detail
KP Module		
RFDet	$H \times W$	RFDet [22]
MP Module		
Distance Encoder	$MN \times L \times 64$	1D Conv + ReLU + DropOut
Motion Encoder	$MN \times L \times 64$	1D Conv + ReLU + DropOut
D-Block	$MN \times L \times 64$	1D Conv + LeakyReLU 1D Conv + LeakyReLU
M-Block	$MN \times L \times 64$	1D Conv + LeakyReLU 1D Conv + LeakyReLU 1D Conv + LeakyReLU
W-Block	$MN \times L \times 1$	1D Conv + SoftMax
DM-Block	$MN \times L \times 64$	1D Conv + LeakyReLU 1D Conv + LeakyReLU
Motion Decoder	$MN \times 1 \times 2$	Linear
TS Module		
Trajectory Encoder	$64 \times E \times M \times N$	Linear + ReLU + DropOut
T-Block	$64 \times E \times M \times N$	3D Conv + ReLU 3D Conv + ReLU 3D Conv + ReLU
Kernel Decoder	$12 \times E \times M \times N$	Linear + Sigmoid
Scale Decoder	$1 \times E \times M \times N$	Linear

We use RFNet [22] as the keypoint detector. Compared with other deep learning-based keypoint detectors such as Superpoints [4] and LFNNet [21], RFDet can generate a high-resolution keypoint map, which is beneficial for accurate homography estimation and keypoint motion propagation in our method.

MP Module. For each frame, there are MN grid vertices, *i.e.*, M vertices in the horizontal direction and N vertices in the vertical direction. In addition, there are L keypoints on the frame. Thereby, the distance vector between each keypoint and vertex can be calculated, which can form a tensor of size $[MN, L, 2]$. Besides, we tile the keypoint motion vectors of size $[L, 2]$ on each frame to have a size of $[MN, L, 2]$. They are fed into two separate encoders in our MP network, *i.e.*, distance encoder and motion encoder. These encoders generate distance feature and motion features with 64 channels, *i.e.*, in the size of $[MN, L, 64]$. Then, they are further processed by the D-Block and M-Block, respectively, to get further feature embeddings, which have the same size as the inputs, *i.e.*, $[MN, L, 64]$. Then, in the top branch, the distance embeddings are fed into the W-Block to generate the distance-aware attention weight of size $[MN, L, 1]$, where the sum of the weight along the L dimension is 1. In the bottom branch, both the distance embeddings and motion embed-

dings are concatenated together to feed into the DM-block for further transformation, where the output feature has a size of $[MN, 1, 64]$. Next, the attention weight is used to aggregate the feature from the bottom branch by weighted sum along the L dimension to get the weighted feature of size $[MN, 1, 64]$. Finally, a linear layer is used as the motion decoder to decode the weighted feature into the residual motion vectors of all vertices of size $[MN, 1, 2]$. Then, we can calculate the motion vectors of all vertices according to Eq. (4) in the paper. The detailed structure of each block in our MP module is presented in Table 7.

TS Module. Once we have the motion vector of each vertex, the trajectory can be obtained by associating the motion vector of corresponding grid vertex on each frame temporally, *i.e.*, $T_k = \{t_{ik} = \sum_{m=1}^i n_{mk} | \forall i \in [1, E]\}$, where E is the number of frames in a video. T_k can be represented as a tensor of size $[2, E, M, N]$. Note that here we use motion profiles to represent the trajectories by following [19]. First, the trajectory is encoded as trajectory feature of size $[64, E, M, N]$ by the trajectory encoder in our CNN-based trajectory smoother. Then, it is further processed both temporally and spatially by the T-Block while keeping the feature size. Next, the transformed feature is further fed into two separate decoders, *i.e.*, the kernel decoder and scale decoder, to generate smoother kernel weight and scale, respectively, where the smoother kernel weight is of size $[12, E, M, N]$ while the smoother scale is of size $[1, E, M, N]$. They are multiplied together in an element-wise manner to get the final smoother kernel weight. To keep consistent with Eq. (9) in the paper, the neighborhood radius is 3. Thereby, there are 12 weights for each vertex since we generate different weights for different dimensions (*i.e.*, horizontal and vertical). In this way, we get the final smoother kernel for the trajectory with different weights at each location and time step, which is aware of the dynamics of each trajectory. The generated weights are used for smoothing the trajectory according to Eq. (9) in the paper. The detailed structure of each block in our TS module is presented in Table 7.

Implementation Details. We used 50 unstable videos from DeepStab [29] as the training data and the other 10 unstable videos as test data. For each video, we randomly clipped 80 consecutive frames for training. Adam optimizer with beta (0.9, 0.99) was used as the optimizer for both MP and TS modules. The MP module was trained with $\lambda_m = 10$ and $\lambda_v = \lambda_s = 40$ for 300 epochs, where the initial learning rate was $2e-4$ and decreased by 0.5 every 100 epochs. The TS module was trained with $\lambda = 15$ and $\lambda_c = 20$ for 330 epochs, where the first 30 epochs are used for warm-up. The learning rate was set to $2e-5$ and decreased by 0.5 every 100 epochs. The total training process took about 15 hours on a single NVIDIA Tesla V100 GPU.

B. User Study

Evaluation of video stabilization is also a subjective task since different subjects may have different visual experience and tolerance on stability, distortion, and cropping ratio. Therefore, we carried out a user study to compare our model with the commercial software Adobe Premiere Pro CC 2019 for video stabilization. Note that, to the best of our knowledge, Adobe Premiere and Adobe After Effects adopt the same stabilizer with the default setting. First, we chose three representative videos from each of the five categories in the NUS [18] dataset to constitute the test videos. 25 subjects participated in our study with ages from 18 to 30. Each subject was aware of the concept of stability, distortion, and cropping ratio after a pre-training phase given some test videos and results by other methods. Then, the stabilized videos generated by our DUT and Adobe Premiere were displayed side-by-side but in random order. Each subject was required to indicate its preference according to the stabilized video quality in terms of the aforementioned three aspects. The final statistics of the user study are summarized in Figure 7. It can be seen that most users prefer our stabilization results than those by Adobe Premiere. We find that since Adobe Premiere uses traditional keypoints detectors, the detected keypoints in consecutive frames may drift as shown in Figure 8, especially in the videos from the quick rotation category, leading to less satisfying stabilization results than our deep learning-based model.

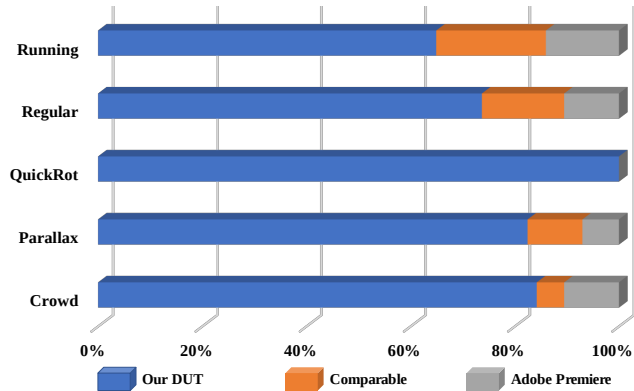


Figure 7. User preference study.

C. Robustness Evaluation

The optical flow calculated by traditional or deep learning-based methods may contain errors in some areas, *e.g.* dynamic objects or textureless regions. To evaluate the robustness of our DUT concerning inaccurate optical flow values, we randomly added noise on the optical flow map and ran our stabilizer based on it accordingly. Three types of noise were included in the experiments, *i.e.*, Gaussian noise (denoting “G”), Salt and Pepper noise (denot-

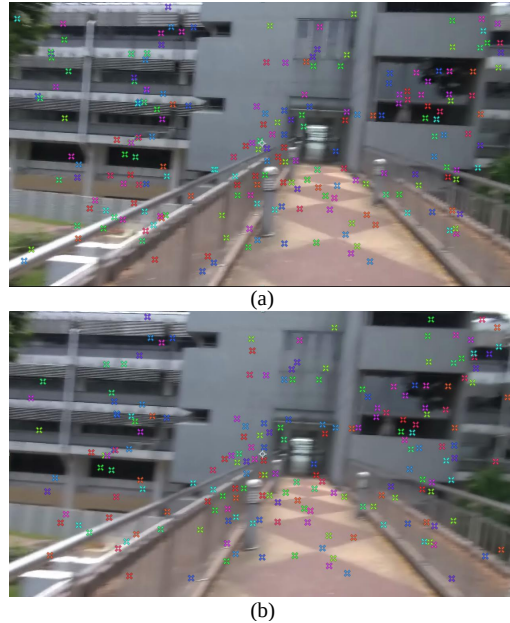


Figure 8. Keypoints detected by Adobe Premiere in two consecutive frames.

Table 8. Robustness evaluation of the proposed DUT with respect to different levels and types of noise. G: Gaussian noise; SP: Salt and Pepper noise.

	Stability \uparrow	Distortion \uparrow	Cropping \uparrow
No-Noise	0.833	0.949	0.704
G-5	0.832	0.949	0.704
G-10	0.832	0.949	0.704
G-15	0.832	0.949	0.704
G-20	0.832	0.949	0.704
SP	0.830	0.948	0.704
Blank	0.831	0.949	0.704

ing “SP”), and the value missing error (denoting “Blank”). Specifically, we added different types of noise on 10% regions randomly chosen from each optical flow map. We set four different levels of standard deviations for the Gaussian noise, *i.e.*, 5% (G-5), 10% (G-10), 15% (G-15), and 20% (G-20) of the maximum flow values. We ran the experiment three times for each setting and calculated the average metrics. The results are summarized in Table 8. As can be seen, our model is robust to various types of noise and different noise levels, *i.e.*, only a marginal performance drop is observed when there is noise in the optical flow map. It can be explained as follows. First, the detected keypoints are always distinct feature points that are easy to get accurate optical flow. Second, the keypoints are distributed sparsely on the image that some of them may not be affected by the randomly added noise. Third, our CNN-based motion propagation module can deal with the noise since it leverages an attention mechanism to adaptively select important keypoints by assigning high weights and aggregate

their motions in a weighted sum manner. Thereby, it can be seen as an adaptive filter to deal with the noise (*i.e.*, inaccurate optical flow values).

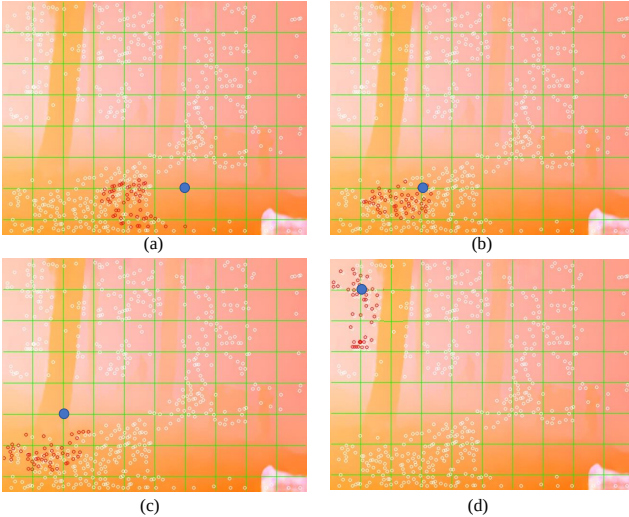


Figure 9. Visualization of the important supporting keypoints of different grid vertices, which have large weights in our MP module. For the grid vertex where there are few keypoints in its neighborhood, *e.g.*, (a), and (c), our motion propagation module tends to rely on those keypoints which have similar motions to the grid vertex. For the grid vertex which is surrounded by rich keypoints, *e.g.*, (b), and (d), our motion propagation module relies more on the nearby keypoints which have similar motions to the grid vertex.

D. More Empirical Studies of the MP Module

D.1. Visual Inspection

To further demonstrate the effectiveness of our MP module, we visualized the important supporting keypoints for some grid vertices selected by the MP module in Figure 9. Note that we sorted the weights of all the keypoints generated by our MP module for each grid vertex, and selected those with large weights as the supporting keypoints as shown in red circles in Figure 9. Other keypoints are marked as white circles. The grid vertex is marked as the blue point. For the grid vertex where there are few keypoints in its neighborhood, *e.g.*, (a) and (c), the MP module prefers choosing those keypoints which have similar motions to the grid vertex. For the grid vertex which is surrounded by rich keypoints, *e.g.*, (b) and (d), the MP module relies more on the keypoints which are nearby and have similar motions to the grid vertex. Compared with the median filter which treats each point in its neighborhood equally, our MP module can adaptively choose the supporting keypoints from all the keypoints for each grid vertex according to their distances and motion patterns.

D.2. Impact of the Loss Weights

To investigate the impact of different terms in the objective function, we carried out an empirical study of the hyper-parameters, *i.e.*, the loss weights of the L1 loss term L_1 and the distortion constraint term L_d . The objective function is reformulated as:

$$L_{MP} = \lambda_1 L_1 + \lambda_2 L_d, \quad (12)$$

$$L_1 = \sum_{i=1}^{E-1} \sum_{k=1}^{MN} \sum_{j \in \Omega_{ik}} \|n_{ik} - m_{ij}\|_1, \quad (13)$$

$$L_d = \lambda_v \sum_{i=1}^{E-1} \sum_{j=1}^L \|p_{ij} + m_{ij} - H_{ij}(p_{ij})\|_2^2 + \lambda_s L_{sp}. \quad (14)$$

We changed the weights of λ_1 and λ_2 and evaluated the MP module on test videos from the regular and parallax categories. Note that λ_v and λ_s were kept 1:1 according to their amplitudes on a subset of training data. The results are plotted in Figure 10. As can be seen, with an increase of λ_1 , both the distortion and distance metrics become marginally better for the regular category, while they become worse for the parallax category. Using a large λ_1 to emphasize L_1 in the objective function, the MP model acts like a median filter, which is not able to deal with multiple planar motions in the videos from the parallax category. By contrast, with an increase of λ_d , our MP model achieves better performance for the parallax category in terms of both distortion and distance metrics. Generally, the MP module is robust to different hyper-parameter settings for the regular category. We set λ_1 as 10 and λ_2 as 40 in other experiments, *i.e.*, $\lambda_m = 10$, $\lambda_v = \lambda_s = 40$.

E. More Empirical Studies of the TS Module

E.1. Impact of the Smoothing Iterations

For most of the stabilization methods, they always need to make a trade-off between stability and distortion (as well as the cropping ratio). Usually, the more stable a stabilized video is, the more distortions (and smaller cropping ratio) it may have. For practical application, one stabilizer may carefully choose hyper-parameters according to users' preference, *e.g.*, higher stability or less distortion. For the trajectory-based method, it is easy to control the stabilization results to match users' preferences by adjusting the smoothing iterations. We call this property a controllable video stabilization. However, other deep learning-based methods that directly predict transformation matrices do not have such a good property. As an example, we investigate the impact of smoothing iterations in our CNN-based TS module and make the trade-off between different metrics. Specifically, we ran our smoother with different iterations,

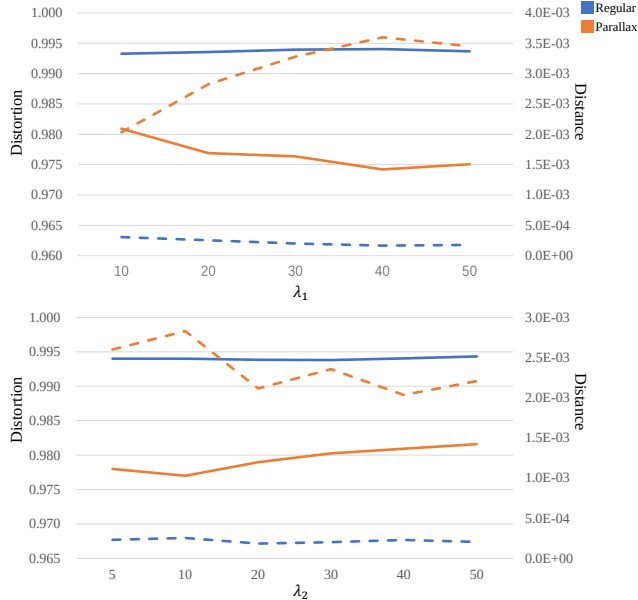


Figure 10. Empirical study of the loss weights in the objective function of the MP module. The solid lines represent the distortion metric and the dashed lines represent the distance metric. Please refer to Section 4.4.1 in the paper.

i.e., 5, 10, 15, 20, 30, 40, 50, 100 and plotted the average stability and distortion scores as well as the cropping ratios on all categories in Figure 11 accordingly.

It can be seen that the stability score increases rapidly at the beginning and then saturate after 15 iterations for all categories. For the distortion and cropping ratio, they decrease fast at the beginning and then decrease slowly. Besides, we plotted the smoothed trajectories using different smoothing iterations for a video from the Regular category in Figure 12, where the front view, profile view, and top view of the trajectories are plotted in (a)-(c), respectively. The unstable trajectory is shown in blue and smoothed trajectories are shown in different colors. As can be seen, with the increase of the iterations, the trajectory becomes more smoothing and deviates from the original trajectory rapidly at the beginning. Then, it changes slowly and converges after a few iterations. Generally, for different categories, there are slightly different critical points that can make a trade-off between these metrics. We choose 15 iterations for all categories according to the average performance to make a trade-off between different metrics as well as keep the computational efficiency of our method.

E.2. Impact of the Loss Weights

In this part, we investigate the impact of different terms in the objective function of the TS module. We carried out an empirical study of the loss weights. The objective func-

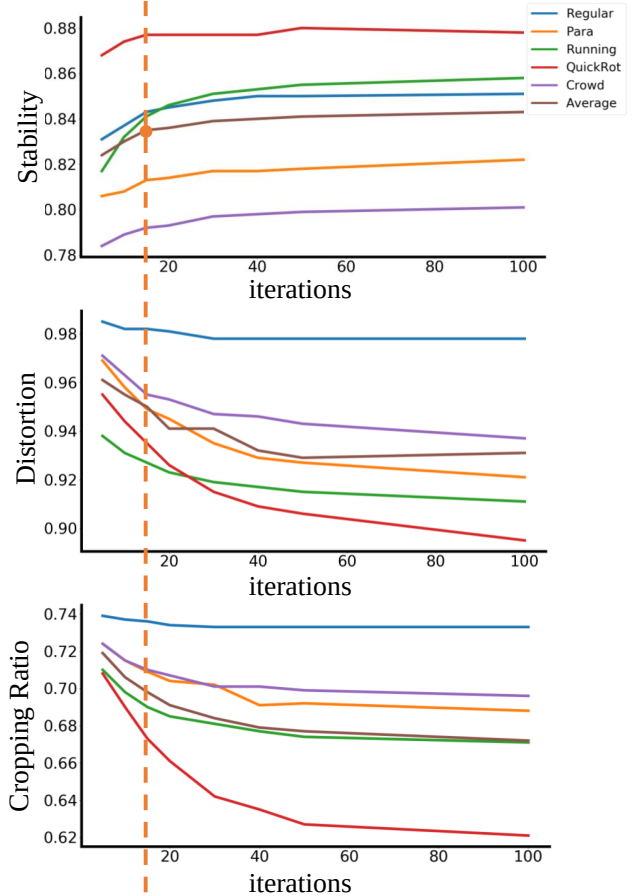


Figure 11. The stability, distortion, and cropping ratio at different settings of smoothing iterations. With the increase of the iterations, the stability score increases rapidly at the beginning and then saturates for all categories. For the distortion and cropping ratio, they decrease fast at the beginning and then saturate or decrease slowly. It is reasonable since more smoothing iterations lead to a more smoothing trajectory which is far away from the original one. We choose 15 iterations as a trade-off between these metrics as indicated by the orange dashed line.

tion was reformulated as:

$$L_{TS} = \sum_{i=1}^{E-1} (\|\widehat{T}_{ik} - T_{ik}\|_2^2 + \lambda_1 L_{smooth} + \lambda_2 L_{distortion}), \quad (15)$$

$$L_{smooth} = \sum_{j \in \Omega_i} w_{ij} \|\widehat{T}_{ik} - \widehat{T}_{jk}\|_2^2, \quad (16)$$

$$L_{distortion} = \lambda_s L_{sp} + \lambda_c L_{cp}. \quad (17)$$

We changed the weights of λ_1 and λ_2 and evaluated the TS module on test videos from the regular and parallax categories. Note that λ_s and λ_c were kept 2:1 according to their amplitudes on a subset of training data. The results are plotted in Figure 13. As can be seen, with the increase of λ_1 , more stable results can be achieved for both categories while the distortion scores decrease, *i.e.*, marginally for the

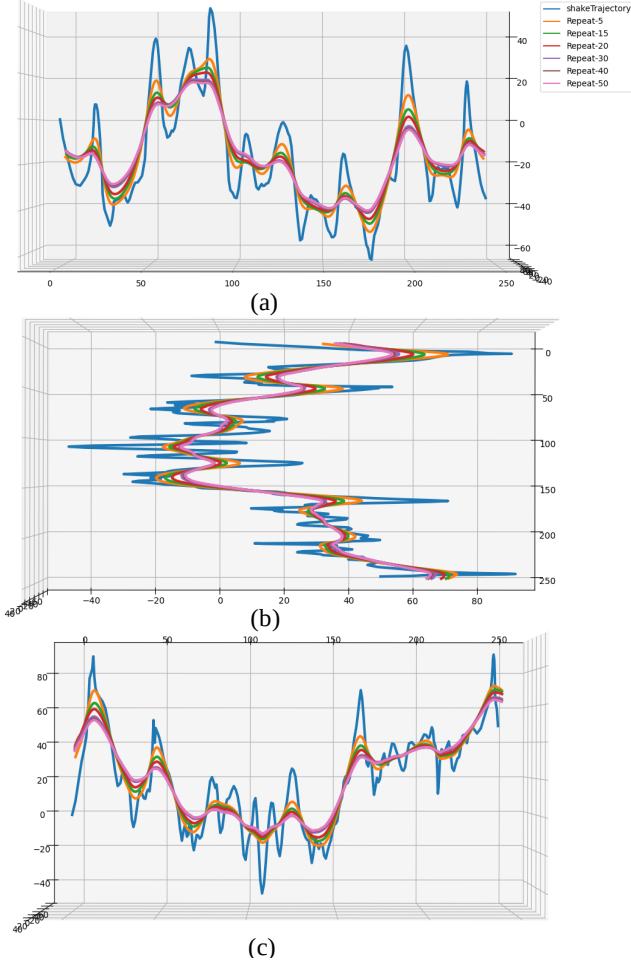


Figure 12. Visualization of the smoothed trajectories using different smoothing iterations. (a) The Front view. (b) The profile view. (c) The top view. The unstable trajectory is shown in blue and smoothed trajectories are shown in different colors. With the increase of the iterations, the trajectory becomes more smoothing and deviates from the original trajectory rapidly at the beginning. Then, it changes slowly and converges after a few of iterations.

Regular category but significantly for the Parallax category. It is reasonable since the distortion term contributes less to the objective function. When varying λ_2 , the stability score does not change a lot while the distortion scores first increase and then decrease at the late stage, especially for the Parallax category. The distortion term encourages the transformation in each grid to keep the grid shape. However, the grid around the boundaries between two planes may not be necessary to keep its shape due to the different planar motions. Thereby, a large distortion term will lead to distortions in these regions. Generally, the TS module is robust to different settings for the regular category. We set λ_1 as 15 and λ_2 as 20 in other experiments, *i.e.*, $\lambda = 15$, $\lambda_s = 40$, and $\lambda_c = 20$.

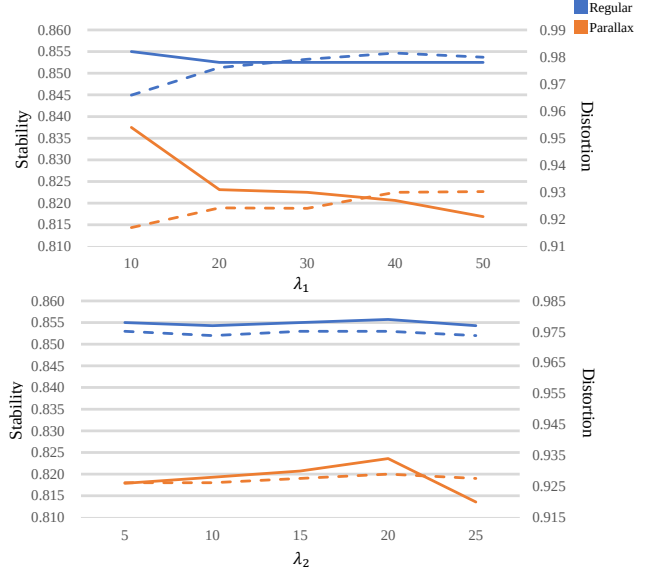


Figure 13. Empirical study of the loss weights in the objective function of the TS module. The solid lines represent the distortion metric and the dashed lines represent the stability metric.

F. More Subjective and Objective Results

Table 9. Stability, Distortion and Cropping ratio metrics regarding the zoom category.

	Stability \uparrow	Distortion \uparrow	Cropping \uparrow
MeshFlow	0.833	0.751	0.532
StabNet	0.804	0.635	0.437
DIFRINT	0.830	0.852	0.813
DUT	0.844	0.954	0.670

We also conducted experiments on unstable videos from the zoom category [18]. These videos contain both extrinsic and intrinsic parameters change. The subjective results are shown in Figure 14. Explicit shear problems can be observed in the results by Meshflow since it treats each frame as a single plane. Subspace also produces large shear distortion due to the unavailable long-term tracked keypoints. The interpolation-based stabilizer DIFRINT produces ghost artifacts around the sharp boundaries. Our DUT model avoids such problem by using the trajectory-based stabilization pipeline and the multi-homography estimation method. The objective metrics are summarized in Table 9. The scores of Subspace are not included since it fails to stabilize some videos in this category. It shows that our DUT model achieves the best performance in terms of stability and distortion and outperforms others by large margins. Our DUT model also obtains the best cropping ratio among the warping-based stabilizers.

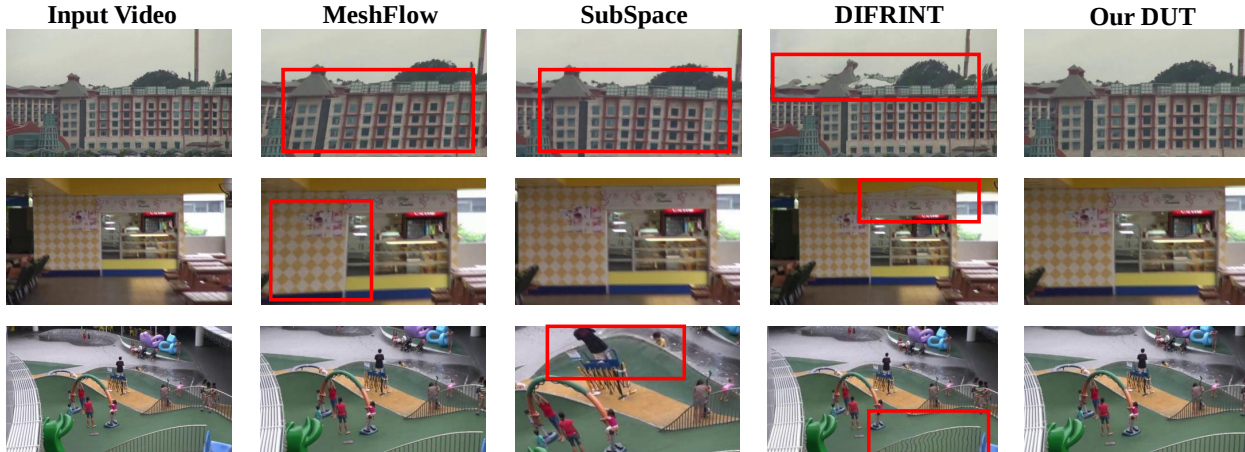


Figure 14. Subjective results of Meshflow [16], Subspace [15], DIFRINT [3] and our DUT on unstable videos from the zoom category.

G. Empirical Study of DUT Framework

Our DUT adopts a representative trajectory-based pipeline which consists of three components: 1) keypoint detection, 2) trajectory estimation based on keypoints and motion, and 3) trajectory smoothing. Each component can use either traditional counterparts or our deep learning based models. To provide a thorough evaluation of the performance of our proposed motion propagation module, trajectory smoothing module, and the total framework, we use different settings of each module and test their performance on the regular category from [18], as shown in Table 10. ‘F’ denotes FAST keypoint detector [28] and ‘R’ denotes RFNet [22]. ‘K’ denotes the KLT tracker and ‘P’ denotes using PWCNet [25]. ‘MF-S/M’ represents using the median filter with single- or multi- homography estimation for motion propagation. ‘MP-S/M’ represents using our motion propagation module with a single- or multi- homography estimation strategy. ‘J’ represents using Jacobi solver for trajectory smoothing with 100 iterations and ‘T’ represents using our trajectory smoothing module with 15 iterations. Total results of 32 variants are available and the average performance is shown in Table 11. **Firstly**, deep learning based keypoint detector is more robust than traditional keypoint detector as the average performance of all metrics are better. **Secondly**, the motion extracted from PWCNet is more appropriate for the stabilization task than the KLT tracker as it can estimate more reliable motion for textureless regions. **Thirdly**, it can be seen that our motion propagation module can obtain better distortion scores than median filter methods in all settings since it can adaptively choose reliable keypoints based on the keypoints’ motions and locations. **Fourthly**, the multi-homography estimation strategy achieves better performance with the incorporation of RFNet and PWCNet as it can better deal with videos with multiple planar motions. **Fifthly**, our trajec-

tory smoothing module can generate better distortion scores while preserving the stability with fewer iterations when the estimated trajectories are accurate. However, inaccurate estimated trajectories may mislead our trajectory smoothing module as the trajectory smoothing module relies on the estimated trajectories for dynamic smoothing. **In conclusion**, our proposed DUT framework with all modules using deep learning-based models achieve the best performance regarding the three metrics.

Table 10. Stability, Distortion and Cropping ratio metrics regarding the regular category.

	Stability↑	Distortion↑	Cropping↑
F+K+MF-S +J	0.811	0.920	0.685
F+K+MF-M+J	0.767	0.780	0.612
F+K+MP-S +J	0.827	0.925	0.684
F+K+MP-M+J	0.809	0.846	0.646
F+K+MF-S +T	0.810	0.915	0.681
F+K+MF-M+T	0.766	0.784	0.604
F+K+MP-S +T	0.826	0.924	0.684
F+K+MP-M+T	0.807	0.838	0.640
F+P+MF-S +J	0.830	0.914	0.704
F+P+MF-M+J	0.765	0.579	0.504
F+P+MP-S +J	0.831	0.918	0.699
F+P+MP-M+J	0.791	0.711	0.558
F+P+MF-S +T	0.830	0.916	0.683
F+P+MF-M+T	0.763	0.573	0.452
F+P+MP-S +T	0.830	0.917	0.702
F+P+MP-M+T	0.782	0.704	0.559
R+K+MF-S +J	0.810	0.948	0.711
R+K+MF-M+J	0.809	0.954	0.712
R+K+MP-S +J	0.818	0.944	0.695
R+K+MP-M+J	0.815	0.940	0.695
R+K+MF-S +T	0.812	0.950	0.710
R+K+MF-M+T	0.809	0.959	0.712
R+K+MP-S +T	0.816	0.943	0.696
R+K+MP-M+T	0.815	0.942	0.696
R+P+MF-S +J	0.842	0.980	0.734
R+P+MF-M+J	0.840	0.978	0.733
R+P+MP-S +J	0.843	0.980	0.735
R+P+MP-M+J	0.843	0.982	0.735
R+P+MF-S +T	0.841	0.980	0.735
R+P+MF-M+T	0.838	0.979	0.733
R+P+MP-S +T	0.843	0.981	0.734
R+P+MP-M+T	0.843	0.983	0.736

Table 11. Average performance of DUT framework regarding the regular category.

	Stability↑	Distortion↑	Cropping↑
F + *	0.803	0.823	0.631
R + *	0.827	0.964	0.719
R + K + *	0.813	0.948	0.703
R + P + *	0.842	0.980	0.734
R + P + MF + *	0.840	0.979	0.734
R + P + MP + *	0.843	0.981	0.735